Three-dimensional tumour microenvironment reconstruction and tumour-immune interactions' analysis

Panagiotis Barmpoutis
Centre for Medical Image Computing
Department of Computer Science
University College London
London, United Kingdom
p.barmpoutis@ucl.ac.uk

Hamzeh Kayhanian
UCL Cancer Institute
Department of Pathology
University College London
London, United Kingdom
h.kayhanian@ucl.ac.uk

William Waddingham
UCL Cancer Institute
Department of Pathology
University College London
London, United Kingdom
w.waddingham@ucl.ac.uk

Daniel C. Alexander
Centre for Medical Image Computing
Department of Computer Science
University College London
London, United Kingdom
d.alexander@ucl.ac.uk

Marnix Jansen
UCL Cancer Institute
Department of Pathology
University College London
London, United Kingdom
m.jansen@ucl.ac.uk

***Abstract*—Tumours arise within complex 3D microenvironments, but the routine 2D analysis of tumours often underestimates the spatial heterogeneity. In this paper, we present a methodology to reconstruct and analyse 3D tumour models from routine clinical samples allowing 3D interactions to be analysed at cellular resolution. Our workflow involves cutting thin serial sections of tumours followed by labelling of cells using markers of interest. Serial sections are then scanned, and digital multiplexed data are created for computational reconstruction. Following spectral unmixing, a registration method of the consecutive images based on a pre-alignment, a parametric and a non-parametric image registration step is applied. For the segmentation of the cells, an ellipsoidal model is proposed and for the 3D reconstruction, a cubic interpolation method is used. The proposed 3D models allow us to identify specific interaction patterns that emerge as tumours develop, adapt and evolve within their host microenvironment. We applied our technique to map tumour-immune interactions of colorectal cancer and preliminary results suggest that 3D models better represent the tumour-immune cells interaction revealing mechanisms within the tumour microenvironment and its heterogeneity.**

Keywords—Tumour microenvironment, tumour-immune cell interactions, multiplex immunofluorescence, three-dimensional model, immune subpopulations.

I. INTRODUCTION

Immune cells infiltrate into the tumour microenvironment and their spatial organization and heterogeneity have been known to have active role in cancer progression and clinical relevance regarding prognosis and response to certain immunotherapies for several human carcinoma types [1]-[3]. Thus, more and more studies are being carried out examining tumour-cell proliferation and survival, tumour angiogenesis and metastasis in accordance with the immune system [4]. As cell count alone might not be able to provide a complete picture of the immune landscape [5], tumour immunologists aim to uncover interactions between tumour and immune cells that may lead to more effective treatment strategies. In general terms, in the most common cancers, including colorectal cancer [6], a tumour microenvironment with a higher immune infiltration including CD8+ and FOXP3+ T cells or low CD4+/CD8+ cells ratio is associated with improved clinical outcomes or prolonged survival [7]-[12].

Nevertheless, the majority of above methods use gene expression deconvolution techniques that lack spatial information. Thus, a comprehensive study of tumour microenvironment necessitates the application of multiplex imaging techniques. These allow the quantification of immune cell subsets as well as the identification of non-tumoural and tumoural cell interactions. Focusing on multiplex immunofluorescence (mIF), this technique is based on the use of fluorophores to visualize the location of bound antibodies. In addition, mIF offers the advantage of large linear dynamic range of most fluorophores allowing the quantitation of marker intensity. Multiplex IF preserves the architectural features of the tumour and reveals the spatial relationships between tumour cells and immune cells. Hence, more recently, numerous studies based on the mIF and two-dimensional (2D) cell models have further investigated the role of immune system aiming to predict and to improve patients' responses to therapies [13]-[18]. These utilize 2D spatial analysis either counting the number of immune cells per slide or in a distance from the nearest tumour cell or estimating the distance between different types of cells or the distance between immune cells and tumour cells.

However, as the tumour microenvironment is known for its complexity, both in its content as well as its dynamic nature, is difficult to study it using 2D cell models [19]. As such, there is considerable interest in 3D models [20], [21] of the tumour microenvironment toward 3D analysis and predicting and monitoring response to therapy. Three-dimensional models offer better geometry, cells interaction representations and intra-tumoural heterogeneity. Moreover, three-dimensional architecture of the tumour microenvironment characterized by a heterogeneous distribution of cells and local features may have functional significance. To date, no generally applicable digital pathology approach has been proposed to generate 3D tumour microenvironment at cellular resolution from mIF image stacks. Towards this end, in this paper we propose a methodology for the generation and analysis of 3D models using mIF. More specifically, this paper makes the following contributions:

- We introduce a methodology for the generation of 3D tumour microenvironment models at cellular resolution from mIF image stacks.

- We compare 2D and 3D tumour-immune cell interactions and we investigate tumours with many immune subpopulations.

Preliminary results suggest that 3D models can better represent the tumour-immune cells interaction and tumour microenvironment heterogeneity. To this end, the proposed 3D models may assist in exploring further the link between immune cell infiltration and tumour prognosis and/or response to therapies.

II. Materials and Methods

The proposed methodology for the mIF 3D tumour microenvironment reconstruction and analysis is shown in Fig. 1. Initially, data preparation and pre-processing were performed including an antibody panel selection followed by immune-staining application, scanning and spectral unmixing. Then, registration of the consecutive mIF samples and single-cell segmentation were applied. Finally, based on the previous steps, 3D reconstruction and three-dimensional cellular organisation analysis were performed.

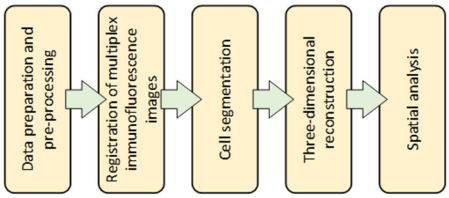

Fig. 1. The proposed workflow.

A. Data preparation and pre-processing

Consecutive tissue sections consisting of more than 25,000 cells and an antibody panel consisting of MSH6, CD20, FOXP3, CD4, PANCK and CD8 were selected for the mIF assay (Table I). The Opal (Akoya) mIF automation kit was used which includes horseradish peroxidase (HRP) con-jugated secondary antibody, Opal fluorophores, DAPI stain, antibody diluents and blocking buffers. The manufacturer's protocol was followed and immuno-staining performed using the Leica Bond RX autostainer (Leica Biosystems). Furthermore, a representative tumour section was labelled with Pan-CK primary antibody and with-out opal fluorophore to assess levels of background autofluorescence. The spectral unmixing library including endmember selection created using 5 epi-fluorescence filters (DAPI, FITC, Cy3, Texas red, Cy5) and thus, contribution of fluorophores to an image channel was expressed as follows:

$$s(\lambda) = \sum \hat{a}_i \times r_i(\lambda) \quad (1)$$

where $s(\lambda)$ is the measured spectrum, coefficients $\hat{a}$ are the contribution of the fluorophores and $r(\lambda)$ represents the spectral contribution of the fluorophores to every channel. Thus, the individual fluorescence signals were estimated by taking into account the total number of spectral channels and adopting a linear least squares approach minimizing the following:

$$min\|s(\lambda) - r(\lambda)\hat{a}\|^2 \quad (2)$$

Following the removal of the estimated autofluorescence, 7 channels were extracted corresponding to the selected antibodies and the DAPI stain (Fig. 2).

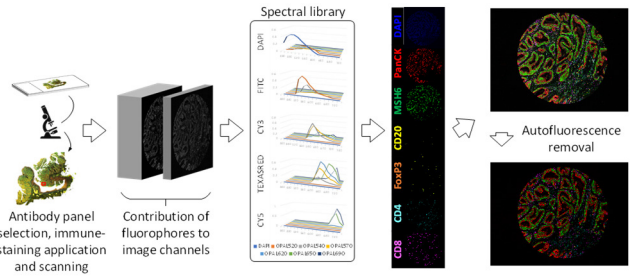

Fig. 2. Data preparation and pre-processing.

Table I	Antibody Panel
PANCK	PanCK is expressed by all normal colon cells and colon cancer cells. PanCK is a cytoplasmic protein.
MSH6	Mismatch repair protein involved in repairing DNA base pair mismatches during cell division. MSH6 is a nuclear protein.
CD20	Marker of B lymphocytes. B lymphocytes form part of the immune system and produce antibodies. CD20 is a cytoplasmic protein.
FOXP3	Marker for T regulatory cells. T cells form part of the immune system. Tregs are a type of T cell have a role in suppressing other types of immune cells. FOXP3 is a nuclear protein.
CD4	Maker of T helper cells. These are a type of T cell that help other immune cells work. CD4 is a cytoplasmic protein.
CD8	Marker of cytotoxic T cells. CD8+ T cells are involved in killing infected cells and cancer cells by producing chemicals that destroy cells detected as foreign. CD8 is a cytoplasmic marker.

B. Registration of multiplex immunofluorescence images

In this workflow we aim to minimize the objective function $J(I_r, I_w, t) \rightarrow min$, where I_r is the reference image, I_w is the warped image and t is the desired transformation. The proposed method consists of a pre-alignment step, a parametric registration following by a non-parametric registration. In the pre-alignment step, based on the selected channel images, the center of tissue samples or tumour microarrays (TMA) is determined by fitting a rectangular in the segmented tissue and estimating the center of it. Then, based on the estimated sizes of reference and template images and their detected centers, size adjustment, translate registration and rotation alignment was performed. In the next step, an affine deformation y of 6 degrees of freedom was applied. Based on the [22] we aimed to minimize the following criterion, with respect to these parameters, by an iterative procedure defined as:

$$ECC(p) = \left\| \frac{\bar{\imath}_r}{\|\bar{\imath}_r\|} - \frac{\bar{\imath}_w(p)}{\|\bar{\imath}_w(p)\|} \right\|^2 \quad (3)$$

where, $\bar{\imath}_r$ and $\bar{\imath}_w(p)$ are the zero mean vectors of the reference vector i_r and the warped vector $i_w(p)$ respectively, p is a vector of unknown parameters and $\|\cdot\|$ denotes the Euclidean norm. To this end, it is considered that the objective function that must be maximized is the enhanced correlation coefficient:

$$\rho(p) = \frac{\bar{\imath}_r^t \bar{\imath}_w(p)}{\|\bar{\imath}_r\| \|\bar{\imath}_w(p)\|} \quad (4)$$

Finally, the non-parametric demons algorithm [23] that combines performance and computational efficiency was used in order to improve the registration outcomes. In the demons algorithm, the forces are inspired by the optical flow

equations [24] and the regularization by a Gaussian smoothing [25]. More specifically, the displacement d' between the warped image (w) and the reference image (r) was computed by using the iterative formula as follows:

$$d'(u,v) = -\frac{(I_w^{(n)}(u,v) - I_r(u,v))\nabla I_r(u,v)}{(\nabla I_r(u,v))^2 + (I_w^{(n)}(u,v) - I_r(u,v))^2} \quad (5)$$

where $I_w^{(n)}$ is the warped image of iteration n, ∇I_r is the gradient of the reference image and (u, v) is the location of each pixel. Afterwards, d was updated and regularized by a Gaussian filter, while $I_w^{(n)}$ was interpolated using $d^{(n)} = d^{(n-1)} + d'$, constructing the image $y_k^{(n+1)}$, until the maximum number of iterations n was met. For both parametric and non-parametric registrations, a computationally multiscale pyramid efficient scheme was used (5 levels were used). This in combination with the Gaussian filter regularization makes the proposed method robust to autofluorescence noise and beneficial for the registration of mIF data.

C. Cell segmentation

For the cellular level analysis, in this study we introduced a fluorescence cell segmentation approach named ORION (FluORescence cell segmentatION) for multispectral immunofluorescence imaging. The proposed method uses an ellipsoidal model [26] to identify individual cells aiming to keep good balance between the estimated cells' shape and overlapping parts of touching cells. For this, we introduce a single validation criterion that aims to exclude noise and non-cell objects. Initially, the unmixed spectral signatures underwent a Gaussian filter with a 5×5 kernel, an adaptive thresholding method and morphological operations aiming to suppress small artifacts. Then, we estimated the distance transformation of the binary image M of p pixels that represents the connected cells and we estimated the regional maxima of this. Then, based on the hypothesis that cells can be spatially modelled as ellipsoids E_C, the pixels of cells were then modelled using a Gaussian distribution estimating the mixture parameters using the expectation-maximization (EM) algorithm.

Having estimated the ellipsoidal model of cells, we need to reject any erroneous seeds from the candidate list and re-estimate the ellipsoidal models for the remaining seeds. For this study, we developed a new fitness validation criterion taking into account the overall combination of ellipses of candidate seeds. More specifically, the proposed criterion aims to keep the cells well-separated and takes into account the binary areas that are included in the estimated ellipses, the total area of the extracted ellipses, as well as the background area that is included in the estimated ellipses and the overlapping parts of the ellipses of the touching cells. Subsequently, we introduced an intensity-based parameter W_I based on the intensity variance of each estimated ellipse aiming to separate the touching cells with different intensity. To this end, the number of candidate seeds and the estimated ellipsoidal components are defined by maximizing the following fitness degree of the 2D cell data mask:

$$\text{Fitness} = max\left(\frac{A_F - A_B - A_T - W_I}{E}\right) \quad (6)$$

where the total area covered by the estimated ellipses is $E = \sum_{p \in M} E_C(p)$, the foreground area of the binary image M that is included in the estimated ellipses is $A_F = \sum_{p=1} M(p)\, E(p)$, the area of the background area of the binary image M that is included in the estimated ellipses is $A_B = \sum_{p=1}[1 - M(p)]\, E(p)$ and the overlapping parts of the ellipses of the touching cells for the total number of the identified ellipses is defined as $A_T = \sum_{i=1} \sum_{p=1} E_{C_i}(p) \cap E_{C_j}(p), j = 1, j \neq i$. The final segmentation of the clustered cells was performed by applying Bayesian classification which assigns each pixel p to cluster C_i with the maximum posterior probability.

D. Three-dimensional reconstruction and spatial analysis

For the 3D rendering and visualization, Avizo software was used. More specifically, once images were processed then both the initial images and the masks of the segmented cells were used to obtain a 3D representation of the immune infiltration and geospatial correlations. For the 3D reconstruction a cubic interpolation method was used. We performed spatial analysis counting the number of immune cells of each subtype within the vicinity of each tumour cell. More specifically, we used the localized segmented cell centres and a radius $R = 25\mu m$ in order to quantify the number of immune cells. We chose this radius as a biologically relevant distance for interaction between tumour cells and immune cells [27]. Thus, we counted the number of the different immune cells that were identified within this radius of each segmented tumour cell.

III. Results

For the evaluation of the proposed workflow, we conducted tests using a numerous of consecutive and non-consecutive mIF images. The goal of this experimental evaluation is three-fold. Initially, we aim to demonstrate that the introduced registration pipeline outperforms state-of-the-art approaches. Secondly, a detailed experimental evaluation of the proposed immunofluorescence single-cell segmentation is performed. Finally, through the proposed workflow tumour-immune interactions of colorectal cancer are analyzed and compared between two and three dimensions.

A. Registration of multiplex immunofluorescence tissue images

Evaluation of the quality of the registration was conducted on 19 mIF image pairs taken from colorectal specimens. To this end, we manually set seven landmarks in each of the 20 images and Median Relative Target Registration Error (MrTRE) of one image pair was estimated based on all landmarks.

$$MrTRE = median\left\{\frac{\|x_l^R - x_l^T\|_2}{d^T}\right\} \quad (7)$$

where x_l^R and x_l^T are the reference landmarks and warped template landmark. The d^T is the diagonal length of the template image. Then, Median of MrTRE and Average of MrTRE throughout all pre-defined landmarks of image pairs were calculated [28]. For the registration and estimation of the registration parameters, DAPI-stained images were used. For the registration of the rest markers the previously estimated parameters were applied.

Fig. 3 shows the evaluation results and the reduction of the error of the registration pipeline. After the registration, landmark errors are equal to $MMrTRE = 0.27\%$ and $AMrTRE = 0.33\%$ in contrast to the median and average errors before the registration that were equal to $MMrTRE = 5.46\%$ and $AMrTRE = 6.61$. In terms of qualitative visual results, Fig. 4 illustrates the visual comparisons of the contribution of each step of the registration approach proposed in this paper.

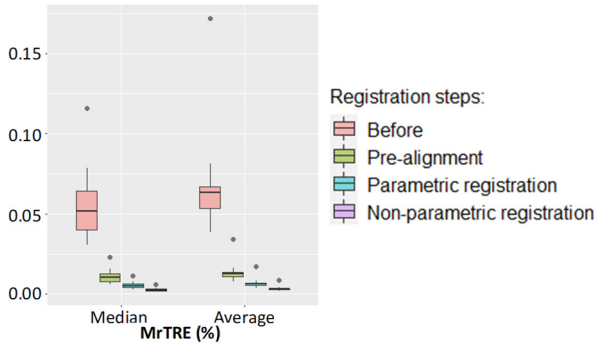

Fig. 3. Median Relative Target Registration Error (Median and Average) rates before alignment and after each registration step.

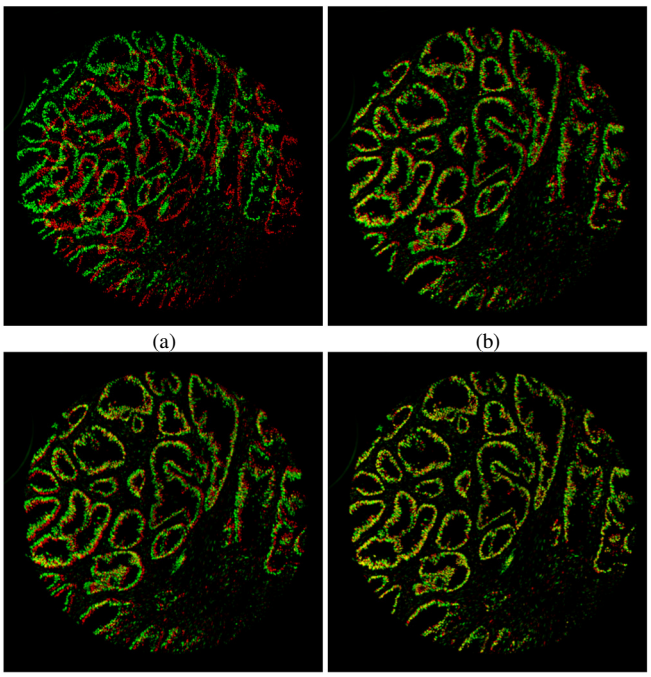

Fig. 4. Qualitative registration results for a pair of images that represents tumour cells before alignment and after each registration step: a) before registration, b) after pre-alignment step, c) after parametric registration, d) after non-parametric registration.

B. *Multiplex immunofluorescence single-cell segmentation*

To evaluate the performance of the proposed cell segmentation method, we conducted tests using a mIF dataset and compared with 4 independent widely-used cell segmentation approaches. More specifically, the dataset of MSI tumours created for this study consists of 400 cells of multiplex IF images. To validate the efficiency of the proposed method we used Jaccard Similarity Coefficient (JSC), as well as Dice false positive (Dice FP) and Dice false negative (Dice FN) values in order to measure over-segmentation and the under-segmentation respectively. Furthermore, Hausdorff distance and mean absolute contour distance (MAD) were used to evaluate the contour of detected cells. It is worth mentioning that the proposed cell segmentation method of different markers was carried out based on nuclear staining or combining DAPI and cytoplasmic staining due to lack of clear cell boundaries (e.g. CD4+ cells).

Table II	**Comparison results on the mIF Dataset**				
	JSC	**MAD**	**Hausdorff**	**DiceFP**	**DiceFN**
Otsu [29]	81.4	5.8	17.5	3.9	17.1
RFOVE [30]	87.1	4.5	7.1	4.8	9.6
Watershed [31]	85.1	4.9	10.1	4.9	10.3
Mask R-CNN [32]	83.7	5.1	10.7	5.2	11.8
ORION (Proposed)	88.2	4.2	6.2	4.5	8.8

The experimental results (Table II) show that the proposed method outperforms four widely-used approaches that have been used in the past for cell segmentation. The introduction of the fitness criterion for the identification of the number of cells in conjunction with the accurate identification of cells' boundaries keep low the Hausdorff rate of the proposed method. On the other hand, the classic watershed algorithm leads to higher oversegmentation results, while the Mask R-CNN which was trained on [32] and fined-tuned on the annotated mIF dataset, needs a higher number of mIF annotated cells in order to perform better.

Finally, we estimated the True Detected Rate in order to determine the ratio of segmented cells number to the total number of annotated cells. It is worth mentioning that the True Detected Rate for the proposed methods was estimated to be equal to 98.9%. Qualitative results of the proposed method are shown in Fig. 5.

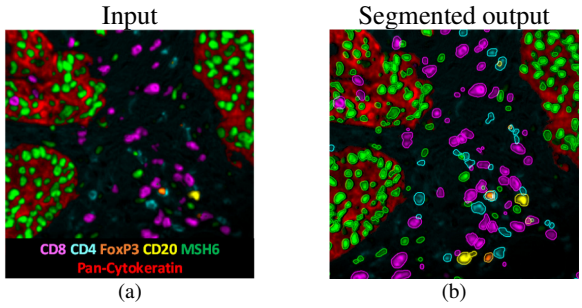

Fig. 5. Qualitative cell segmentation results of the proposed fluorescence cell segmentation approach on the mIF Dataset.

C. *Three-dimensional spatial analysis*

Using the workflow detailed here and the 3D tumour microenvironment reconstructions (Fig. 6), we were able to both quantify tumour-immune cell interactions and their spatial patterns within the tumours. Thus, we analyzed the geospatial correlations of more than 25,000 tumour and immune cells and we compared the tumour-immune cell interactions in the neighbourhood of each tumour cell between two and three dimensions. More specifically, taking into account the two-dimensional analysis, each tumour cell has on average 0.09 CD20 cells, 0.22 FOXP3 cells, 0.22 CD4 cells and 1.49 CD8 cells in its neighbourhood area while for three-dimensional model each tumour cell has on average 0.042 CD20 cells, 0.09 FOXP3 cells, 0.11 CD4 cells and 0.46 CD8 cells in its neighbourhood area (Table III).

Further to this analysis as previously has been reported, low CD4+/CD8+ ratio in the tumour-infiltrating lymphocytes significantly contributes to higher five-year survival in patients [10]. Thus, we compared this ratio between two-dimensional and three-dimensional models. Counting the average ratio value that is associated with improved clinical outcomes, CD4+/CD8+ for two-dimensional models is 0.15 and for three-dimensional models is 0.24. This indicates that three-dimensional analysis provides additional information about the tumour immune microenvironment which may have prognostic implications if validated in larger studies.

Table III	Tumour-immune cell interactions (normalized values)			
	CD20	FOXP3	CD4	CD8
2D spatial analysis	0.09	0.22	0.22	1.49
3D spatial analysis	0.042	0.09	0.11	0.46

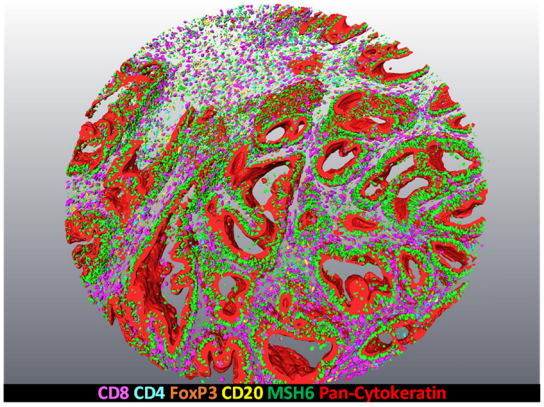

Fig. 6. Three-dimensional tumour microenvironment reconstruction.

Finally, based on the neighbourhood analysis we counted the number of different immune cells within the radius of each tumour cell. Thus, we compared the immune cells correlations between two-dimensional and three-dimensional models aiming to reveal the immune landscape in colorectal cancer. To this end, the Pearson correlation coefficient was used. More specifically, Fig. 7 presents that in both two-dimensional and three-dimensional models there is a moderate to strong association between FOXP3 and CD4 cells, consistent with the presence of a population of regulatory T-cells. In contrast, there was no correlation captured between CD20 and FOXP3 or between CD20 and CD4 within the vicinity of each tumour cell in two-dimensional modelling.

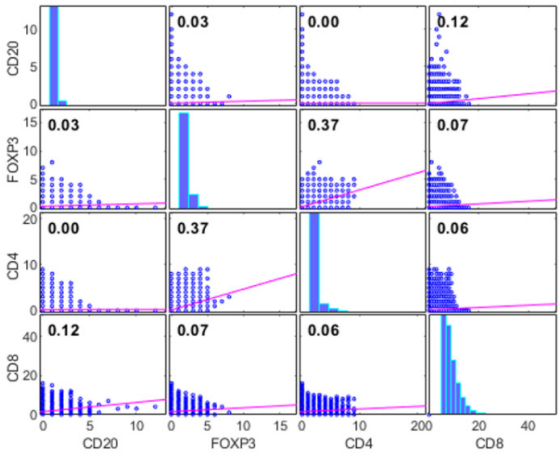

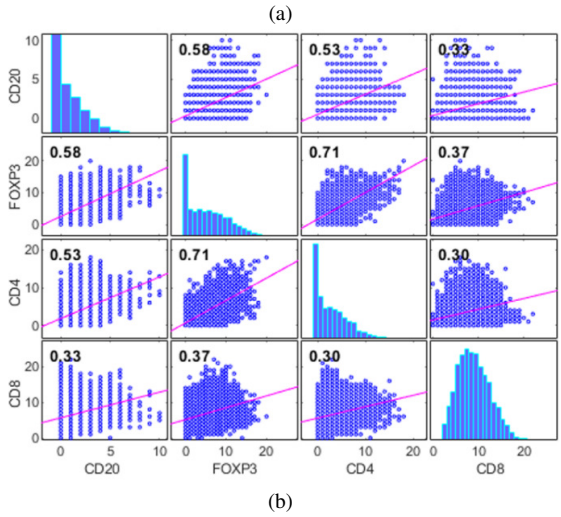

Fig. 7. Comparison of immune cells correlations in (a) two-dimension and (b) three-dimension analysis.

However, in three-dimensional models there was moderate correlation. This correlation can be also validated from the 3D reconstruction in Fig. 8, which show that CD20, FOXP3 and CD4 are present in nearby regions of the examined tumour. This suggests that 3D models can better represent the tumour-immune cells interaction and tumour microenvironment heterogeneity. However, further studies are needed to clarify the scientific mechanism behind these results and insights on tumour immunity in colorectal cancer.

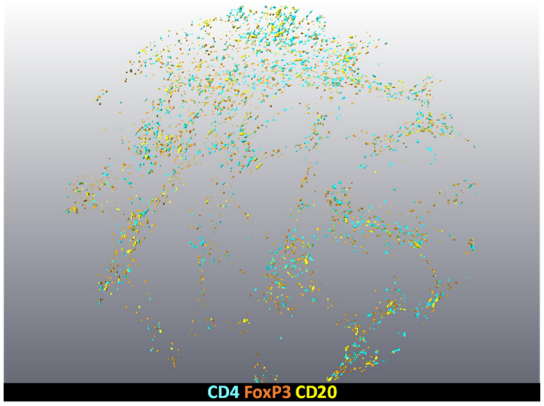

Fig. 8. Three-dimensional reconstruction for: A) CD4, B) FoxP3 and C) CD20.

IV. Conclusion

In this paper, we presented a digital pathology methodology for mIF three-dimensional tumour microenvironment reconstruction and analysis allowing high detail 3D tumour-immune interactions to be visualised and analysed at cellular resolution. The main advantage of the proposed workflow is that tumour-immune interactions are mapped and analyzed in three dimensions allowing better identification of tumour-immune interactions patterns within their host microenvironment. We applied our technique to colorectal cancer microenvironment and preliminary results show that 3D models can better represent the tumour-immune cells interaction and tumour microenvironment heterogeneity. In the future, more mIF data will be collected. This will allow us to study anti-tumour immune responses inside patients' tumours and to compare between treatment responders and non-responders.

ACKNOWLEDGEMENT

We acknowledge the department of Pathology, of UCL Cancer Institute and the UCL Centre for Medical Image Computing. This study was funded by EPSRC, Grant number: NS/A000069/1.

REFERENCES

[1] Yu, *H., Kortylewski, M., Pardoll, D.: Crosstalk between cancer and immune cells: role of STAT3 in the tumour microenvironment. Nature reviews immunology. 7(1): 41-51 (2007).*

[2] *Kather, JN., Suarez-Carmona, M., Charoentong, P., Weis, CA., Hirsch, D., Bankhead, P., Horning, M., Ferber, D., Kel, I., Herpel, E., Schott, S.: Topography of cancer-associated immune cells in human solid tumors. Elife. 4;7: e36967 (2018).*

[3] *Schwen, LO., Andersson, E., Korski, K., Weiss, N., Haase, S., Gaire, F., Hahn, HK., Homeyer, A., Grimm, O.: Data-driven discovery of immune contexture biomarkers. Frontiers in oncology. 18;8: 627 (2018).*

[4] *Hanahan, D., Weinberg, RA.: The hallmarks of cancer. cell. 7;100(1): 57-70 (2000).*

[5] *Morihiro, T., Kuroda, S., Kanaya, N., Kakiuchi, Y., Kubota, T., Aoyama, K., Tanaka, T., Kikuchi, S., Nagasaka, T., Nishizaki, M., Kagawa, S.: PD-L1 expression combined with microsatellite instability/CD8+ tumor infiltrating lymphocytes as a useful prognostic biomarker in gastric cancer. Scientific reports. 15;9(1): 1-9 (2019).*

[6] *World Health Organization, "Cancer", https://www.who.int/news-room/fact-sheets/detail/cancer, last accessed 2021/05/29*

[7] *Galon, J., Costes, A., Sanchez-Cabo, F., Kirilovsky, A., Mlecnik, B., Lagorce-Pagès, C., Tosolini, M., Camus, M., Berger, A., Wind, P., Zinzindohoué, F.: Type, density, and location of immune cells within human colorectal tumors predict clinical outcome. Science. 29;313(5795): 1960-4 (2006).*

[8] *Pagès, F., Kirilovsky, A., Mlecnik, B., Asslaber, M., Tosolini, M., Bindea, G., Lagorce, C., Wind, P., Marliot, F., Bruneval, P., Zatloukal, K. In situ cytotoxic and memory T cells predict outcome in patients with early-stage colorectal cancer. Journal of clinical oncology. 10;27(35): 5944-51 (2009).*

[9] *Menon, AG., Janssen-van Rhijn, CM., Morreau, H., Putter, H., Tollenaar, RA., van de Velde, CJ., Fleuren, GJ., Kuppen, PJ.: Immune system and prognosis in colorectal cancer: a detailed immunohistochemical analysis. Laboratory investigation. 84(4): 493-501 (2004).*

[10] *Diederichsen, AC., Hjelmborg, JV., Christensen, PB., Zeuthen, J., Fenger, C.: Prognostic value of the CD4+/CD8+ ratio of tumour infiltrating lymphocytes in colorectal cancer and HLA-DR expression on tumour cells. Cancer Immunology, Immunotherapy. Jul 1;52(7):423-8 (2003).*

[11] *Salama, P., Phillips, M., Grieu, F., Morris, M., Zeps, N., Joseph, D., Platell, C., Iacopetta, B.: Tumor-infiltrating FOXP3+ T regulatory cells show strong prognostic significance in colorectal cancer. Journal of clinical oncology. 10;27(2): 186-92 (2009).*

[12] *Correale, P., Rotundo, MS., Del Vecchio, MT., Remondo, C., Migali, C., Ginanneschi, C., Tsang, KY., Licchetta, A., Mannucci, S., Loiacono, L., Tassone, P.: Regulatory (FoxP3+) T-cell tumor infiltration is a favorable prognostic factor in advanced colon cancer patients undergoing chemo or chemoimmunotherapy. Journal of immunotherapy. 33(4): 435 (2010).*

[13] *Lu, S., Stein, JE., Rimm, DL., Wang, DW., Bell, JM., Johnson, DB., Sosman, JA., Schalper, KA., Anders, RA., Wang, H., Hoyt, C.: Comparison of biomarker modalities for predicting response to PD-1/PD-L1 checkpoint blockade: a systematic review and meta-analysis. JAMA oncology. 1;5(8): 1195-204 (2019).*

[14] *Lee, CW., Ren, YJ., Marella, M., Wang, M., Hartke, J., Couto, SS.: Multiplex immunofluorescence staining and image analysis assay for diffuse large B cell lymphoma. Journal of immunological methods. 1;478: 112714 (2020).*

[15] *Goltsev, Y., Samusik, N., Kennedy-Darling, J., Bhate, S., Hale, M., Vazquez, G., Black, S., Nolan, GP.: Deep profiling of mouse splenic architecture with CODEX multiplexed imaging. Cell. 9;174(4): 968-81 (2018).*

[16] *Mistry, S., Dakshinamoorthy, G., Singh, J., Nikulina, N., Kim, J., Bashier, R., Gallina, ME., Kennedy-Darling, J.: Highly multiplexed single-cell spatial analysis of tissue specimens using CODEX. 130-23 (2019).*

[17] *Francisco-Cruz, A., Parra, ER., Tetzlaff, MT., Wistuba, II.: Multiplex immunofluorescence assays. Biomarkers for Immunotherapy of Cancer. 467-95 (2020).*

[18] *Fassler, DJ., Abousamra, S., Gupta, R., Chen, C., Zhao, M., Paredes, D., Batool, SA., Knudsen, BS., Escobar-Hoyos, L., Shroyer, KR., Samaras, D.: Deep learning-based image analysis methods for brightfield-acquired multiplex immunohistochemistry images. Diagnostic pathology. 15(1): 1-1 (2020).*

[19] *Hoarau-Véchot, J., Rafii, A., Touboul, C., Pasquier, J.: Halfway between 2D and animal models: are 3D cultures the ideal tool to study cancer-microenvironment interactions?. International journal of molecular sciences. 19(1): 181 (2018).*

[20] *Di Modugno F, Colosi C, Trono P, Antonacci G, Ruocco G, Nisticò P. 3D models in the new era of immune oncology: focus on T cells, CAF and ECM. Journal of Experimental & Clinical Cancer Research. 38(1):1-4 (2019).*

[21] *Jaffe J, Waddingham W, Barmpoutis P, Jansen, M,: Investigating clonal expansions in the normal stomach and the 3D architecture of oxyntic gastric glands. Gut 70:A20-A21 (2021).*

[22] *Evangelidis, GD., Psarakis, EZ.: Parametric image alignment using enhanced correlation coefficient maximization. IEEE Transactions on Pattern Analysis and Machine Intelligence. 12;30(10): 1858-65 (2008).*

[23] *Thirion, JP.: Image matching as a diffusion process: an analogy with Maxwell's demons. Medical image analysis. 1;2(3): 243-60 (1998).*

[24] *Barron, J.L., Fleet, D.J. and Beauchemin, S.S.: Performance of optical flow techniques. International journal of computer vision, 12(1): 43-77 (1994).*

[25] *Vercauteren, T., Pennec, X., Perchant, A. and Ayache, N.: Diffeomorphic demons: Efficient non-parametric image registration. NeuroImage, 45(1): S61-S72 (2009).*

[26] *Dimitropoulos, K., Barmpoutis, P., Koletsa, T., Kostopoulos, I., Grammalidis, N.: Automated detection and classification of nuclei in pax5 and H&E-stained tissue sections of follicular lymphoma. Signal, Image and Video Processing. 1;11(1): 145-53 (2017).*

[27] *Chakiryan, N.H., Kimmel, G.J., Kim, Y., Hajiran, A., Aydin, A.M., Zemp, L., Katende, E., Nguyen, J., Lopez-Blanco, N., Chahoud, J. and Spiess, P.E.:. Spatial clustering of CD68+ tumor associated macrophages with tumor cells is associated with worse overall survival in metastatic clear cell renal cell carcinoma. PloS one, 16(4), p.e0245415 (2021).*

[28] *Borovec, J., Kybic, J., Arganda-Carreras, I., Sorokin, DV., Bueno, G., Khvostikov, AV., Bakas, S., Eric, I., Chang, C., Heldmann, S., Kartasalo, K.: ANHIR: automatic non-rigid histological image registration challenge. IEEE transactions on medical imaging. 7;39(10): 3042-52 (2020).*

[29] *Liao, M., Zhao, YQ., Li, XH., Dai, PS., Xu, XW., Zhang, JK., Zou, BJ.: Automatic segmentation for cell images based on bottleneck detection and ellipse fitting. Neurocomputing. 15;173: 615-22 (2016).*

[30] *Panagiotakis, C., Argyros, A.: Region-based Fitting of Overlapping Ellipses and its application to cells segmentation. Image and Vision Computing, 93, 103810, (2020).*

[31] *Viratham Pulsawatdi, A., Craig, SG., Bingham, V., McCombe, K., Humphries, MP., Senevirathne, S., Richman, SD., Quirke, P., Campo, L., Domingo, E., Maughan, TS.: A robust multiplex immunofluorescence and digital pathology workflow for the characterisation of the tumour immune microenvironment. Molecular oncology. 14(10):2384-402 (2020).*

[32] *Caicedo, JC., Goodman, A., Karhohs, KW., Cimini, BA., Ackerman, J., Haghighi, M., Heng, C., Becker, T., Doan, M., McQuin, C., Rohban, M.: Nucleus segmentation across imaging experiments: the 2018 Data Science Bowl. Nature methods. 16(12): 1247-53 (2019).*